

Supplementary Information

Direct Imaging of Lattice Planes in Atomically Precise Noble Metal Cluster Crystals Using a Conventional Transmission Electron Microscope

Ananthu Mahendranath,^{a,b,c} Biswajit Mondal,^{a,b} Korath Shivan Sugi^{a,b} and Thalappil Pradeep^{a,b,*}

^a DST Unit of Nanoscience and Thematic Unit of Excellence, Department of Chemistry, Indian Institute of Technology Madras, Chennai 600036, India.

^b Centre of Excellence on Molecular Materials and Functions, Indian Institute of Technology Madras, Chennai 600036, India.

^c Department of Metallurgical and Materials Engineering, Indian Institute of Technology Madras, Chennai 600036, India.

*Email: pradeep@iitm.ac.in

Table of Contents

Name	Description	Page No.
	Experimental Section	1
	Instrumentation	2
Table S1	Instrument specifications and conditions used for TEM imaging	3
Figure S1	Characterization of cubic Ag ₂₉ clusters	4
Figure S2	Characterization of trigonal Ag ₂₉ clusters	4
Figure S3	Characterization of Ag ₂₅ clusters	5
Table S2	Structural parameters of Ag ₂₉ C crystal from SCXRD	6
Table S3	Structural parameters of Ag ₂₉ T crystal from SCXRD	6

Figure S4	Optical images from sample preparation	7
Figure S5	Additional TEM images from Ag ₂₉ C crystallites	8
Figure S6	Time dependent exposure images of a cubic Ag ₂₉ crystallite	9
Figure S7	TEM image of a crystallite after approximately 56s exposure to electron beam	9
Figure S8	Time dependent exposure images of another cubic Ag ₂₉ crystallite	10
Figure S9	TEM images from thicker Ag ₂₉ C crystallites	11
Figure S10	Fused nanoparticles imaged with lattice resolution	11
Figure S11	Additional TEM Images from Ag ₂₉ T crystallites	12
Figure S12	Time dependent exposure images trigonal Ag ₂₉ T crystallites	13
Figure S13	Additional TEM Images from Ag ₂₅ crystallites	14
Figure S14	TEM images from Ag ₂₉ C crystallites dispersed in water	15
	Calculation of theoretical lattice spacing for various planes	16
Table S4	Lattice spacing of some selected planes in Ag ₂₉ C	16
Table S5	Lattice spacing of some selected planes in Ag ₂₉ T	17
Table S6	Lattice spacing of some selected planes in Ag ₂₅	18
Figure S15	Calculation of experimental lattice spacing for various planes	19

Experimental Section

Chemicals. Sodium borohydride (NaBH_4 , 99.99% metal basis), triphenylphosphine (TPP), tetraphenylphosphonium bromide, benzene-1,3-dithiol (BDT), and 2,4-dimethylbenzenethiol (DMBT) were purchased from Sigma-Aldrich. Silver nitrate (AgNO_3 , 99%) was purchased from RANKEM India. All solvents including methanol, dichloromethane (DCM), and dimethylformamide (DMF) were of analytical grade.

Synthesis of $[\text{Ag}_{29}(\text{BDT})_{12}\text{TPP}_4]^{3-}$ nanocluster. Synthesis of Ag_{29} nanocluster was performed by following a previously reported procedure.¹ 20 mg of AgNO_3 was dissolved in 5 mL of methanol. To this, 10 mL of DCM and 13.5 μL of BDT were added. The solution changed to turbid yellow color on addition of BDT. After stirring for about 2 min, 200 mg of TPP (dissolved in 1 mL of DCM) was added. The turbid yellow color changed to colorless immediately after addition of TPP. After 15 min, 10.5 mg of NaBH_4 in 500 μL of cold deionized (DI) water was added. The stirring was continued for 3 h under dark conditions. The resulting solution was centrifuged, and the supernatant was discarded. The residue was repeatedly washed with methanol to remove excess thiols and thiolates, and was subsequently dispersed in DMF. This DMF dispersion on centrifugation gave cluster alone in the supernatant, and any resulting precipitate was discarded. This purified cluster solution in DMF was dried over glass slides, under dark conditions.

Synthesis of $[\text{Ag}_{25}(\text{DMBT})_{18}]^-$ nanocluster. Synthesis of Ag_{25} nanocluster was performed by following a previously reported procedure.² ~ 38 mg of AgNO_3 was dissolved in 2 mL of methanol. To this, ~ 90 μL of DMBT was added that produced a thick yellow mixture. Next, 17 mL of DCM was added to the vial and stirred for 20 minutes under an ice-bath. A freshly prepared solution of ~ 6 mg tetraphenylphosphonium bromide in 0.5 mL methanol was added before the drop-wise addition of 0.5 mL of ice-cold water containing ~ 15 mg NaBH_4 . Color of the reaction mixture changed to light yellow and then to dark. This solution was allowed to stir for 6 h and aged overnight at 4 $^\circ\text{C}$. Afterward, the dark solution was centrifuged and thus obtained supernatant was concentrated to 5 mL by solvent evaporation in a rotavapor. The cluster was precipitated in methanol, and subsequently washed a couple times in the same solvent. The precipitate obtained was then dissolved into DCM that produced a yellowish Ag_{25} clusters.

Crystallization of Ag_{29}C nanocluster. The purified cluster powder (~ 10 mg) was dissolved in 1 ml of DMF and filtered using a syringe filter. This concentrated cluster solution was drop-casted on a microscope glass slide and was left to evaporate slowly in a dark box, at room temperature. After 2–3 days, luminescent red crystals suitable for SCXRD were obtained.

Crystallization of Ag_{29}T nanocluster. The purified cluster powder (~ 5 mg) was dissolved in 500 μl of DMF and filtered using a syringe filter. The concentrated cluster solution was kept for vapor diffusion with methanol (1.5 ml). After almost 2 months, luminescent red crystals suitable for SCXRD were obtained.

The crystals were also confirmed by monitoring the birefringence using a polarization microscope, for a faster assortment. Trigonal crystals alone showed strong birefringence.

Crystallization of Ag₂₅ nanocluster. The purified cluster powder (~30 mg) was dissolved in 1 ml of DCM and filtered using a syringe filter. The concentrated cluster solution was layered with hexane and kept at 4 °C, under dark conditions. After few days, thick rectangular-shaped black crystals suitable for SCXRD were obtained.

Instrumentation

UV–Visible absorption spectra of all samples were collected using a PerkinElmer Lambda 25 spectrometer.

Electrospray Ionization Mass Spectrometry (ESI MS) of samples were measured using a Waters Synapt G2-Si high-resolution mass spectrometer.

Optical micrograph images were taken on a Leica DM750 P microscope (transmission mode) and Keyence VHX-950F digital microscope (reflection mode).

Scanning Electron Microscopy (SEM) was done using the Helios G4 UX DualBeam microscope.

Single-Crystal X-ray Diffraction (SCXRD) of the nanocluster single crystals were performed on a Bruker D8 VENTURE APEX3 CMOS diffractometer using Cu K α (λ = 1.54178 Å) radiation.

Transmission electron microscopy (TEM) images were taken on a JEOL 3010 microscope. Details are presented below.

Table S1 Instrument specifications and conditions used for TEM imaging

Instrument Model	JEOL 3010 (instrument was purchased in 2004)
Accelerating voltage	100 kV
Beam Current	39 μ A
Frame exposure	0.1 s
Filament	LaB ₆
Camera	Gatan Orius SC200 CCD camera (2K x 2K)
Vaccum	10 ⁻⁵ to 10 ⁻⁶ Pa
Resolution	1.4 Å lattice, 1.2 Å point-to-point
Objective lens	Focal length 2.5mm, Cs 0.6mm, Cc 1.3mm, minimum focus step 1 nm

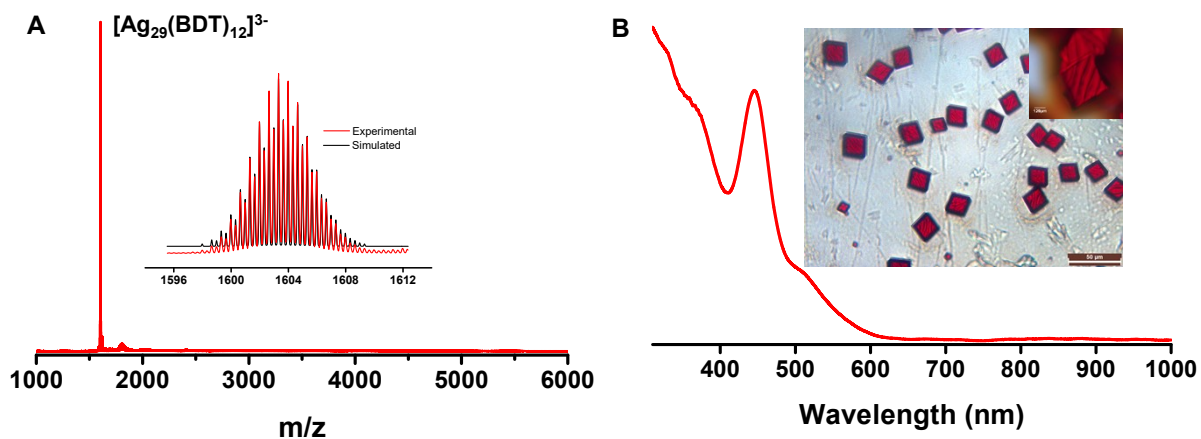


Fig. S1 Characterization of cubic Ag_{29} clusters. (A) Negative mode ESI MS of $[\text{Ag}_{29}(\text{BDT})_{12}(\text{TPP})_4]^{3-}$. Inset shows a comparison between experimental and simulated isotopic distributions of the main peak. (B) UV-Vis absorption spectrum of $[\text{Ag}_{29}(\text{BDT})_{12}(\text{TPP})_4]^{3-}$, dispersed in DMF. Inset shows optical micrograph images taken from a batch of Ag_{29}C crystals.

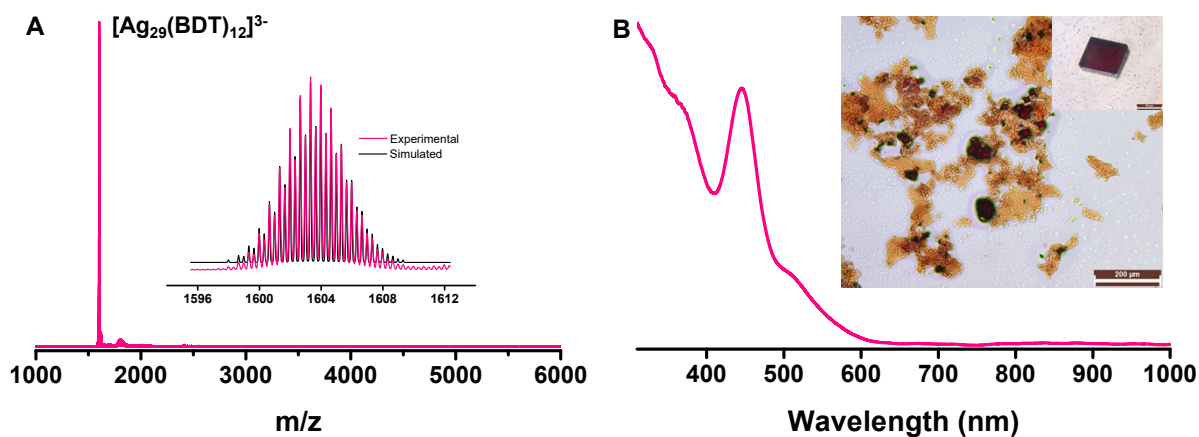


Fig. S2 Characterization of trigonal Ag_{29} clusters. (A) Negative mode ESI MS of $[\text{Ag}_{29}(\text{BDT})_{12}(\text{TPP})_4]^{3-}$. Inset shows a comparison between experimental and simulated isotopic distributions of the main peak. (B) UV-Vis absorption spectrum of $[\text{Ag}_{29}(\text{BDT})_{12}(\text{TPP})_4]^{3-}$, dispersed in DMF. Inset shows an optical micrograph taken from a batch of Ag_{29}T crystals.

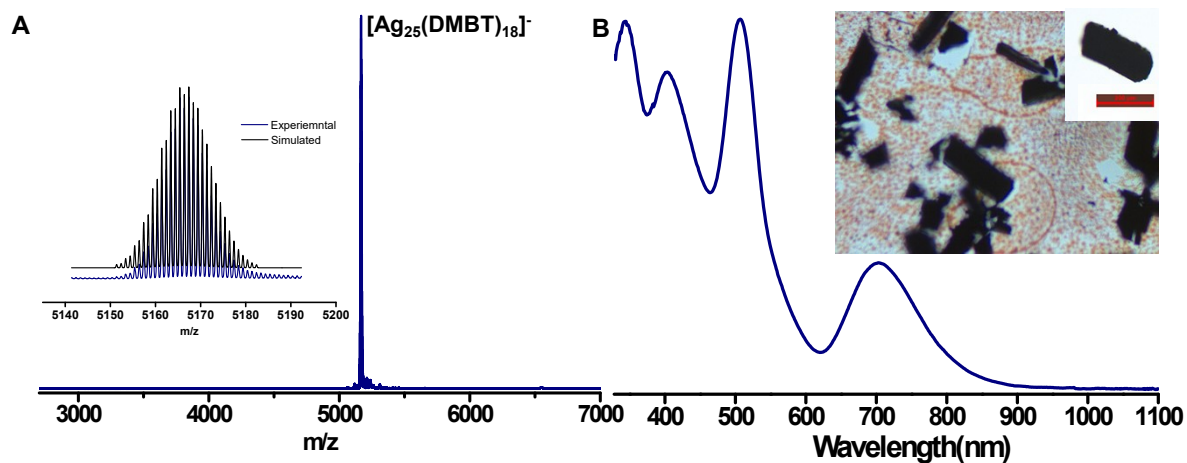


Fig. S3 Characterization of Ag_{25} clusters. (A) Negative mode ESI MS of $[Ag_{25}(DBMT)_{18}]^-$. Inset shows a comparison between experimental and simulated isotopic distributions of the peak. (B) UV-Vis absorption spectrum of $[Ag_{25}(DBMT)_{18}]^-$, dispersed in DCM. Inset shows optical micrograph images taken from a batch of Ag_{25} crystals.

Table S1 Structural parameters of Ag₂₉C crystal from SCXRD

Crystal system	Cubic	
Space group	P a -3	
Unit cell dimensions	a = 34.72 Å	$\alpha = 90^\circ$
	b = 34.72 Å	$\beta = 90^\circ$
	c = 34.72 Å	$\gamma = 90^\circ$
Volume	41841 Å ³	

Table S2 Structural parameters of Ag₂₉T crystal from SCXRD

Crystal system	Trigonal	
Space group	R -3 H	
Unit cell dimensions	a = 27.39 Å	$\alpha = 90^\circ$
	b = 27.39 Å	$\beta = 90^\circ$
	c = 47.66 Å	$\gamma = 120^\circ$
Volume	30967 Å ³	

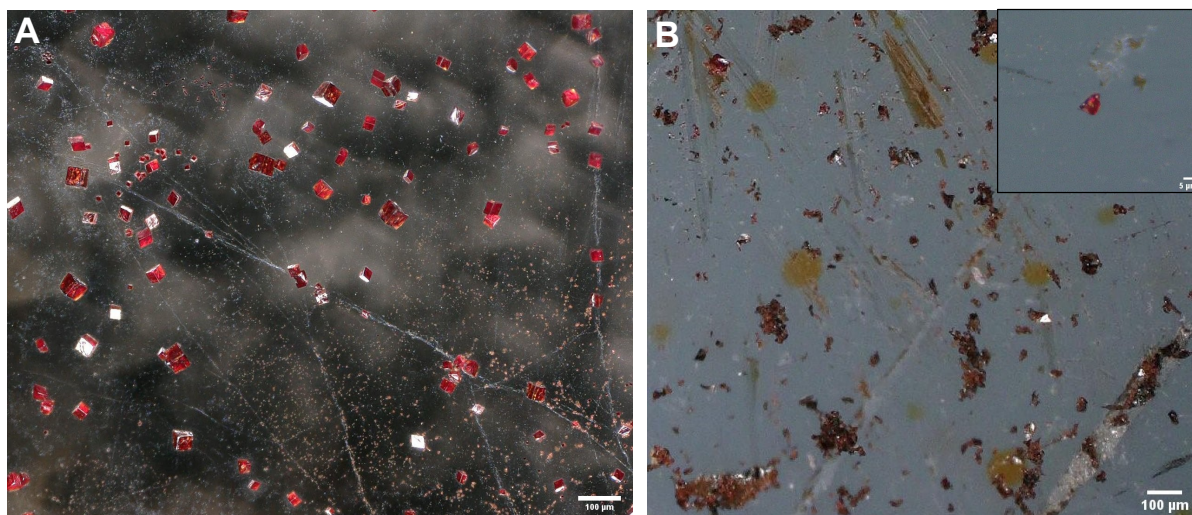


Fig. S4 Optical images of sample preparation. (A) Ag₂₉C crystals before crushing and (B) crushed Ag₂₉C crystallites in the mortar. Inset shows one of the crystallites. The images were recorded in reflection mode.

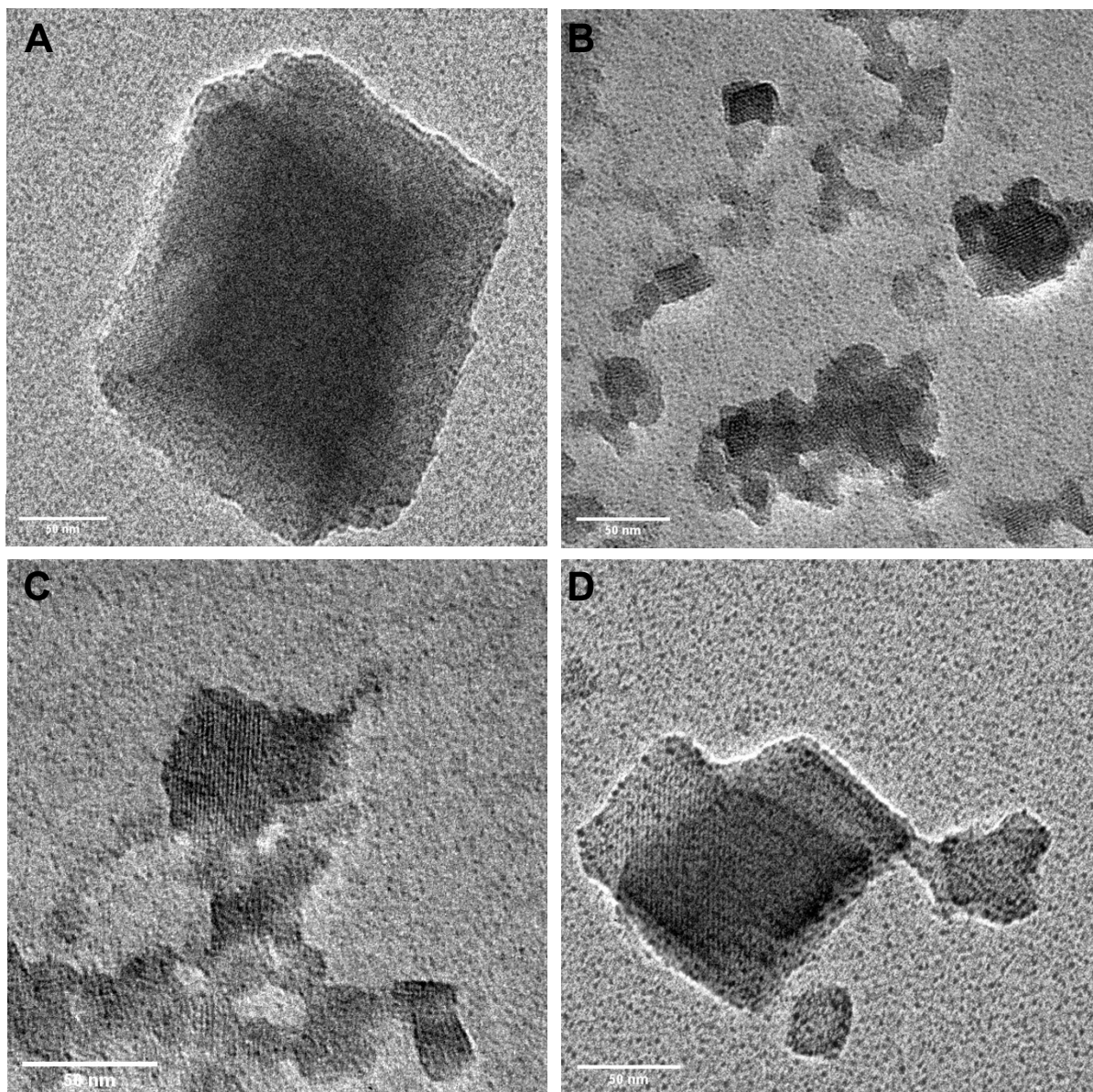


Fig. S5 TEM images from Ag₂₉C crystallites. Early signs of beam induced nanoparticle formation can be seen in D.

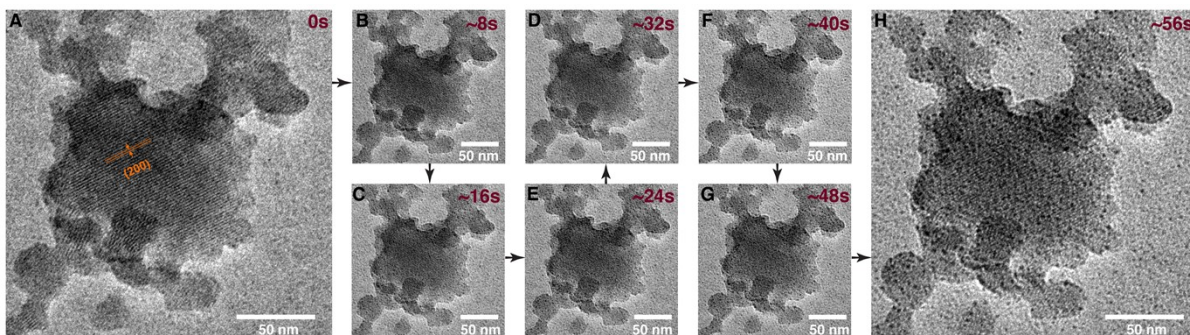


Fig. S6 Systematic transformation in a piece of Ag_{29}C crystal, during extended exposure. Time of exposure is mentioned on the images.

At the beginning of imaging there is hardly any noticeable particle growth on the crystallites. As the experiment advanced, the time through which the crystallite is exposed to the electron beam increases, and we start seeing noticeable particle growth on the crystallites. After approximately 56s, there is considerable particle growth.

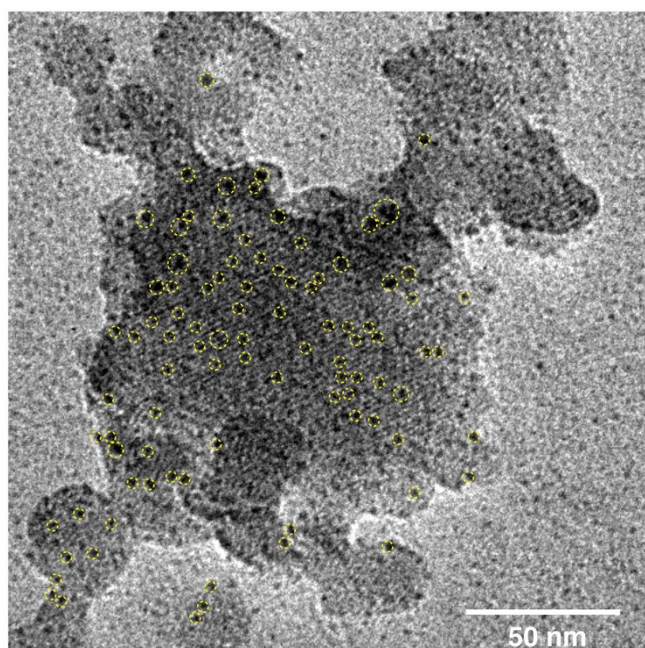


Fig. S7 TEM image of a crystallite after approximately 56s exposure to electron beam. A few of the particles are highlighted. Particles of different sizes, varying from 0.2 nm to 3.8 nm are visible.

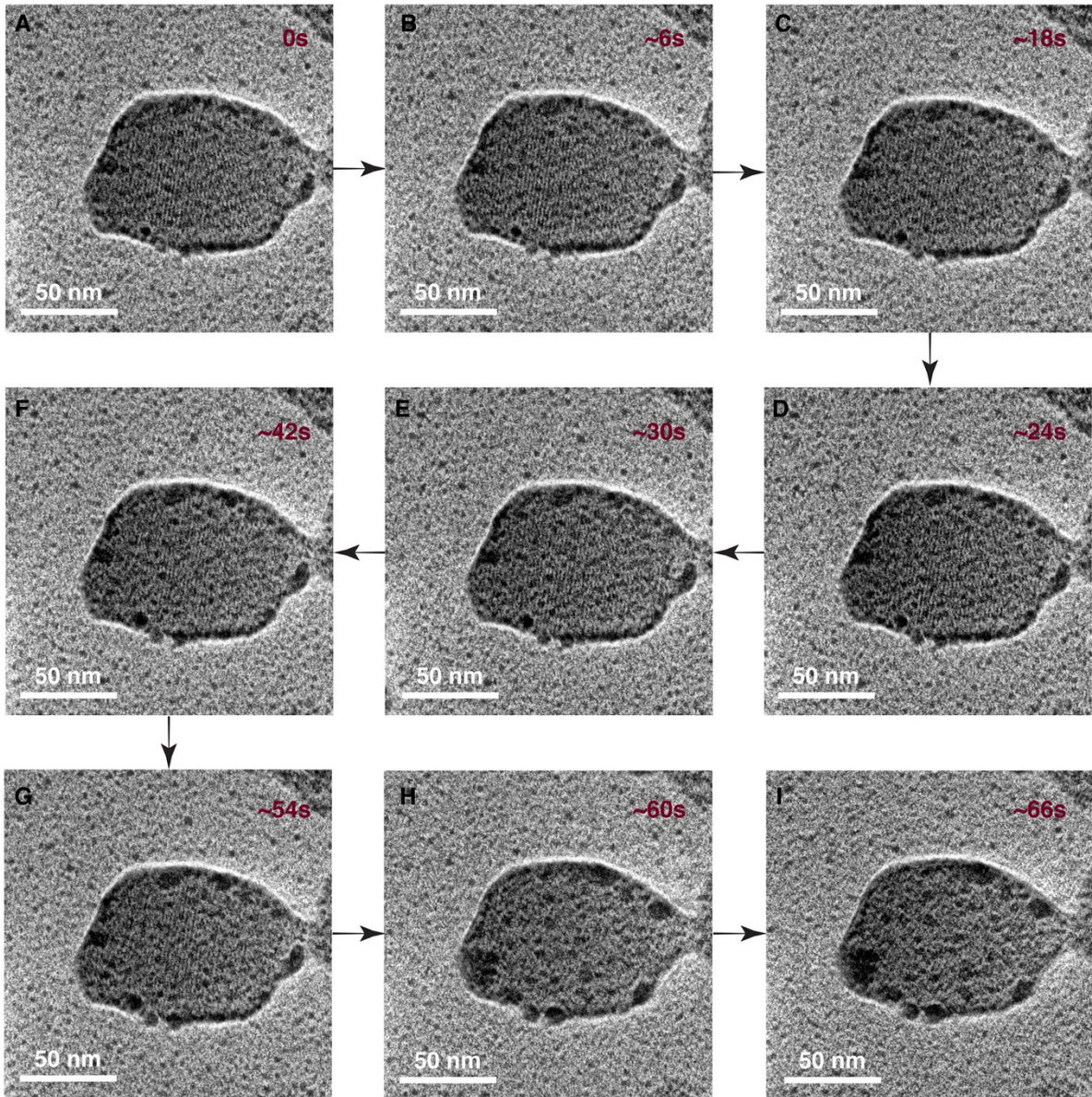


Fig. S8 Systematic transformation in another Ag_{29}C crystallite, during extended exposure. Time of exposure is mentioned on the images.

Beyond approximately 60s, the particle growth becomes predominant and lattice planes of cluster crystals are no more imageable.

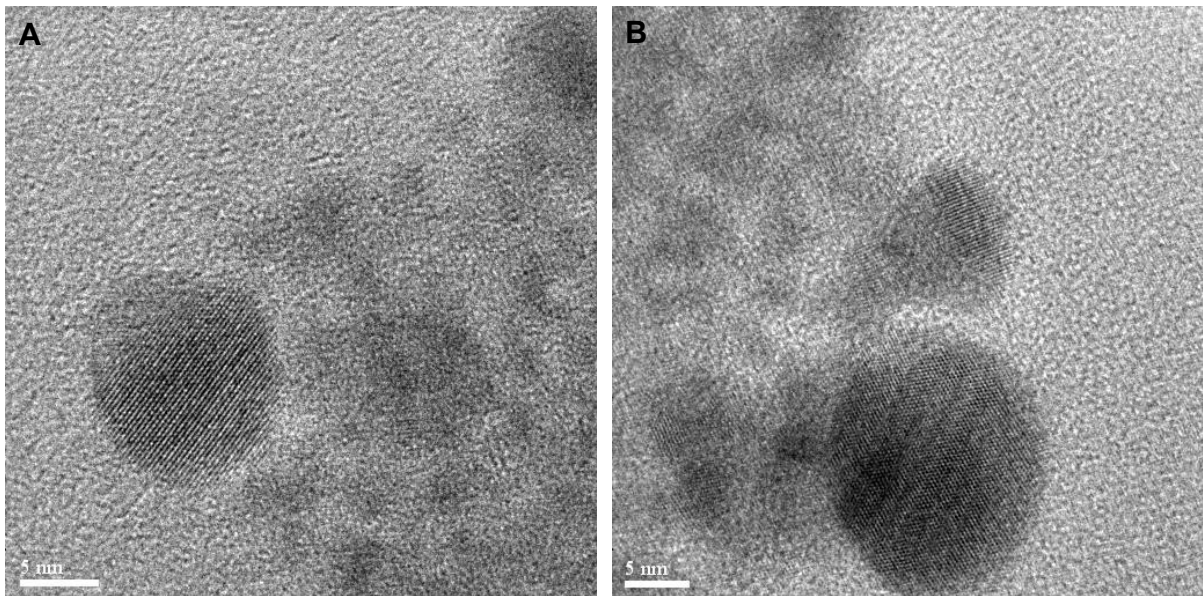


Fig. S9 Fused nanoparticles formed upon exposure beyond ~ 2 min, showing lattice resolution.

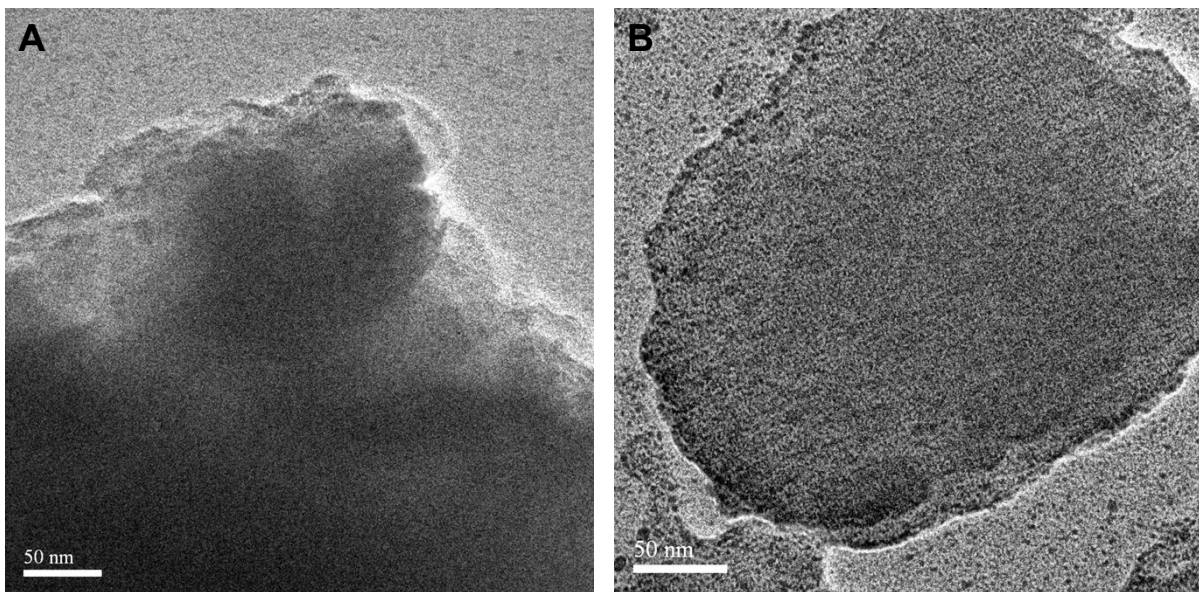


Fig. S10 TEM images from thicker Ag_{29}C crystallites. The electron beam was opaque to these crystallites.

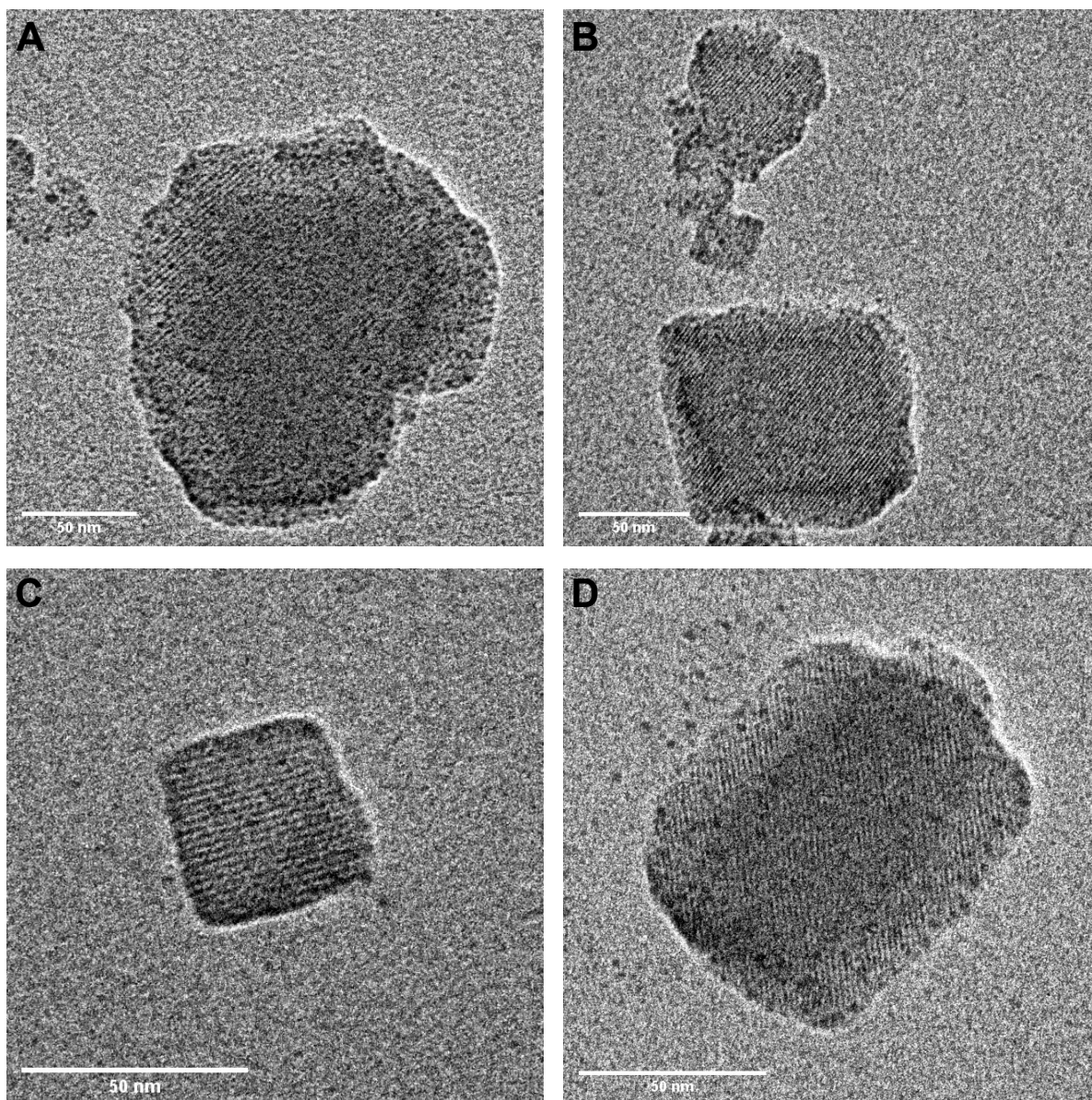


Fig. S11 TEM images from Ag_{29}T crystallites. Early signs of beam induced nanoparticle formation can be seen in all crystallites.

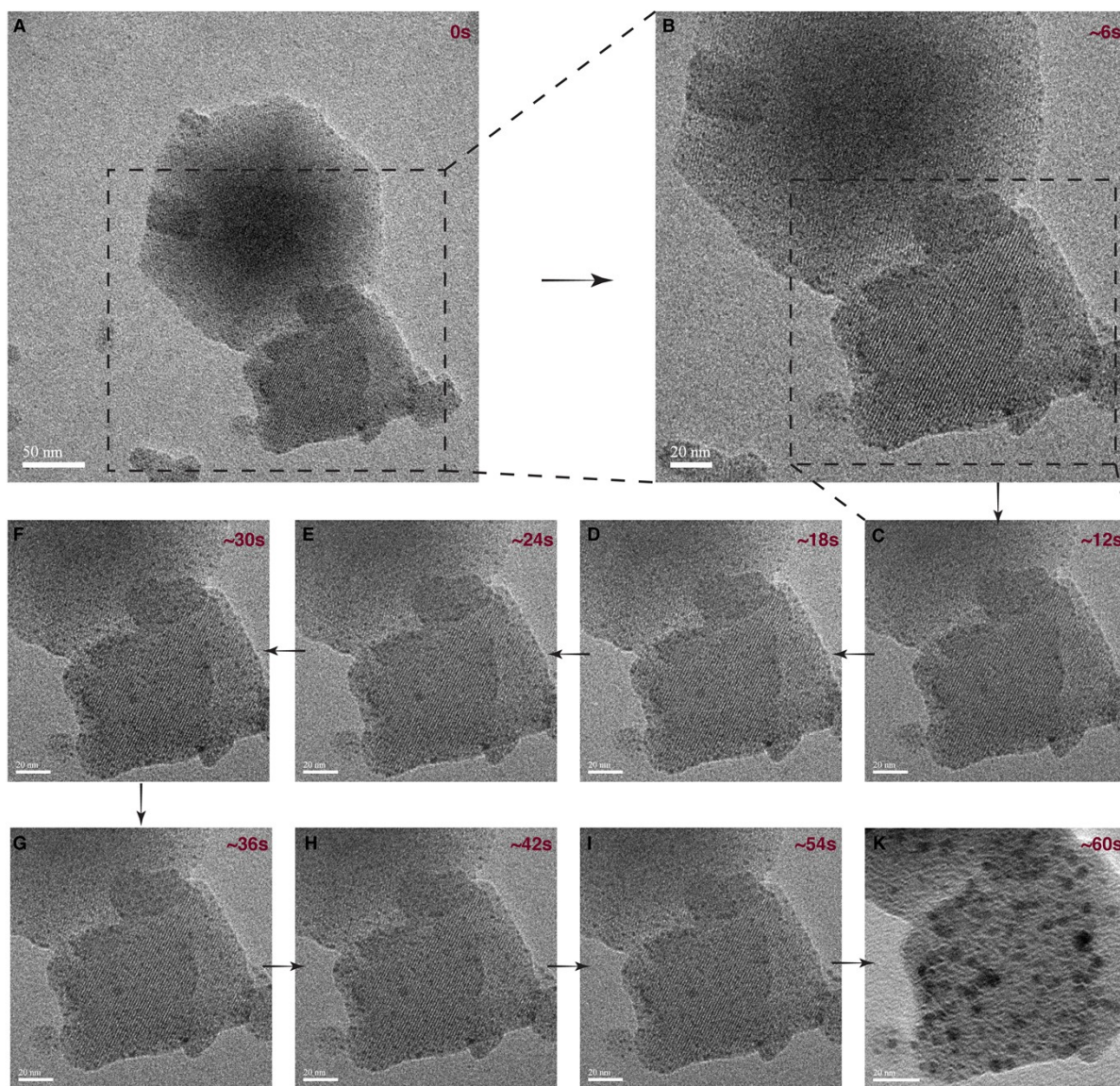


Fig. S12 Systematic transformation happening to an Ag_{29}T crystallite, during extended exposure.

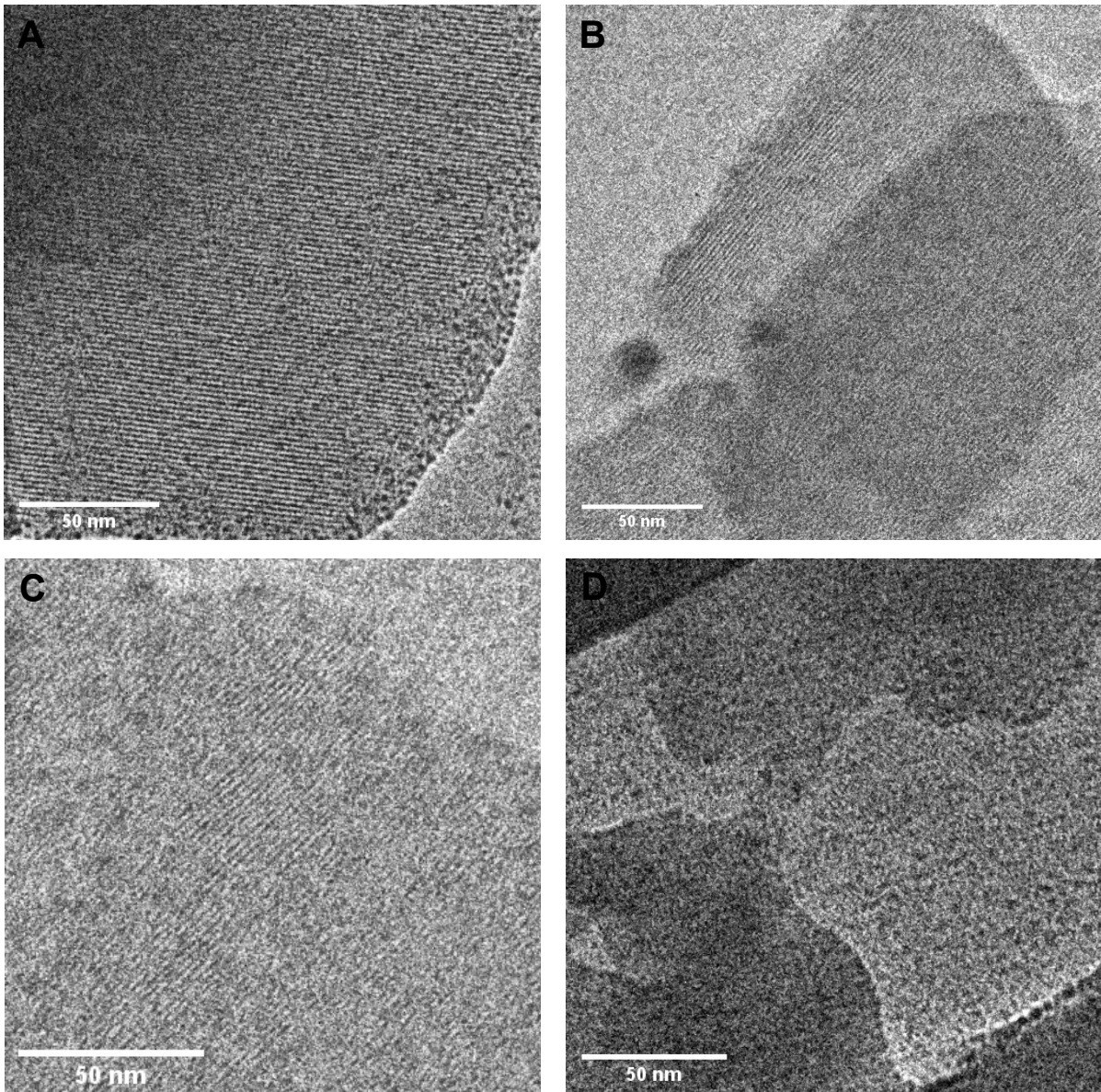


Fig. S13 TEM images from Ag₂₅ crystallites. Early signs of beam induced nanoparticle formation can be seen in (A) and (D).

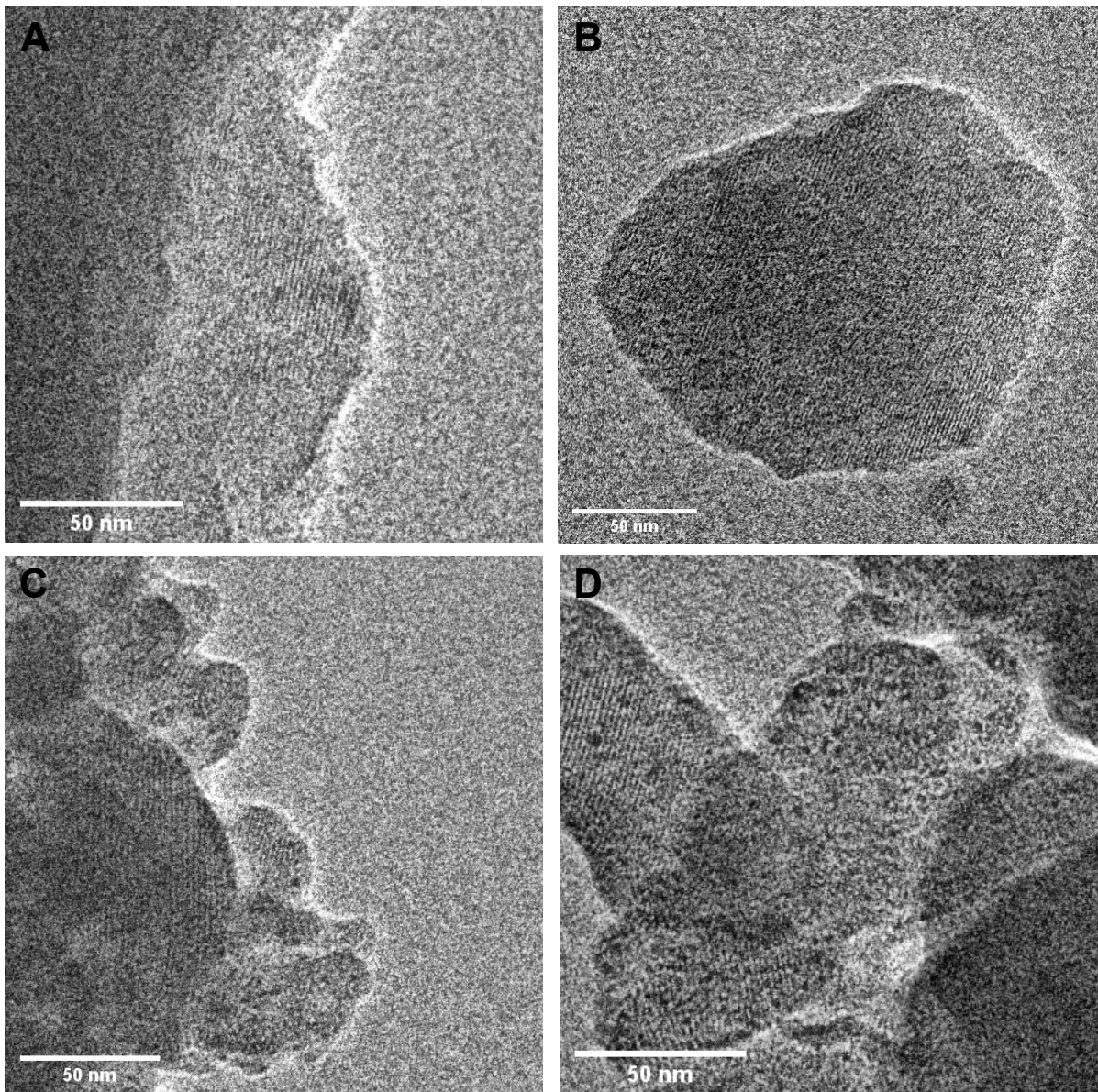


Fig. S14 TEM images of Ag₂₉C crystallites dispersed in water. Beam induced damage is seen in D.

Calculation of theoretical lattice spacing for various planes

The theoretical lattice spacing in various planes in Ag₂₉C, Ag₂₉T and Ag₂₅ were calculated from the standard formula corresponding to their crystal symmetry.

Ag₂₉C has a cubic symmetry, so the following formula was used:

$$\frac{1}{d^2} = \frac{h^2 + k^2 + l^2}{a^2}$$

The following crystal parameters, as reported,¹ were use:

$$a = b = c = 34.2011 \text{ \AA}$$

$$\alpha = \beta = \gamma = 90^\circ$$

Table S4 Lattice spacing of some selected planes in Ag₂₉C

(hkl)	d (nm)
(100), (010), (001), ($\bar{1}00$), ($0\bar{1}0$), ($00\bar{1}$)	3.42
(110), (101), (011), ($\bar{1}10$), ($\bar{1}01$), ($01\bar{1}$), ($1\bar{1}0$), ($10\bar{1}$), ($0\bar{1}1$), ($\bar{1}\bar{1}0$), ($\bar{1}0\bar{1}$), ($0\bar{1}\bar{1}$)	2.42
(111), ($\bar{1}\bar{1}\bar{1}$), ($\bar{1}11$), ($1\bar{1}1$), ($11\bar{1}$), ($\bar{1}\bar{1}1$), ($\bar{1}1\bar{1}$), ($11\bar{1}$)	1.97
(200), (020), (002), ($\bar{2}00$), ($0\bar{2}0$), ($00\bar{2}$)	1.71
(210), (201), (021), (120), (102), (012), ($\bar{2}10$), ($\bar{2}01$), ($01\bar{2}$), ($\bar{1}20$), ($\bar{1}02$), ($02\bar{1}$), ($2\bar{1}0$), ($20\bar{1}$), ($02\bar{1}$), ($01\bar{2}$), ($\bar{2}\bar{1}0$), ($\bar{2}0\bar{1}$), ($0\bar{2}\bar{1}$), ($\bar{1}\bar{2}0$), ($\bar{1}0\bar{2}$), ($0\bar{1}\bar{2}$)	1.52

Ag₂₉T has a trigonal symmetry, so the following formula for a hexagonal lattice was used:

$$\frac{1}{d^2} = \frac{4}{3} \left(\frac{h^2 + hk + l^2}{a^2} \right) + \frac{l^2}{c^2}$$

The following crystal parameters, as reported,³ were used:

$$a = b = 27.46 \text{ \AA}$$

$$c = 46.65 \text{ \AA}$$

$$\alpha = \beta = 90^\circ$$

$$\gamma = 120^\circ$$

Table S5 Lattice spacing of some selected planes in Ag₂₉T

(hkl)	d (nm)
(100), (010), ($\bar{1}00$), ($0\bar{1}0$),	2.38
(011), (101), ($0\bar{1}\bar{1}$), ($\bar{1}0\bar{1}$), ($0\bar{1}1$), ($\bar{1}01$)	2.12
(012), ($10\bar{2}$), ($\bar{1}0\bar{2}$), ($0\bar{1}2$), ($\bar{1}02$), ($0\bar{1}2$), (102), (012)	1.66
(110), ($\bar{1}\bar{1}0$), ($2\bar{1}0$), ($\bar{1}20$), (210), (120)	1.373

Ag₂₅ has a triclinic symmetry, so the following formula was used:

$$\frac{1}{d^2} = \frac{1}{V^2} (S_{11}h^2 + S_{22}k^2 + S_{33}l^2 + 2S_{12}hk + 2S_{23}kl + 2S_{13}hl)$$

where

$$S_{11} = b^2c^2\sin^2\alpha$$

$$S_{22} = a^2c^2\sin^2\beta$$

$$S_{33} = a^2b^2\sin^2\gamma$$

$$S_{12} = abc^2(\cos\alpha\cos\beta - \cos\gamma)$$

$$S_{23} = a^2bc(\cos\beta\cos\gamma - \cos\alpha)$$

$$S_{13} = ab^2c(\cos\gamma\cos\alpha - \cos\beta)$$

The following crystal parameters, as reported,² were used

$$a = 19.0634 \text{ \AA}$$

$$b = 19.5919 \text{ \AA}$$

$$c = 26.7981 \text{ \AA}$$

$$\alpha = 93.424^\circ$$

$$\beta = 90.859^\circ$$

$$\gamma = 104.756^\circ$$

$$V = 9656.7 \text{ \AA}^3$$

Table S6 Lattice spacing of some selected planes in Ag₂₅

(hkl)	d (nm)
(010), (0 $\bar{1}$ 0)	1.89
($\bar{1}$ 00), (100)	1.84
(0 $\bar{1}$ 1), (01 $\bar{1}$)	1.59

$(10\bar{1}), (\bar{1}01)$	1.53
----------------------------	------

Calculation of experimental lattice spacing for various planes

The TEM images were analysed using ImageJ software. The scale bar is calibrated from the value obtained from TEM. Following this, a fast Fourier transform (FFT) pattern was generated from the area where lattice planes were observed. An inverse FFT pattern was generated by selecting an appropriate spot from the FFT pattern. In this inverse FFT pattern, the lines correspond to the lattice planes. A plot profile corresponding to a line drawn perpendicular to the pattern can be generated from which lattice distance was calculated.

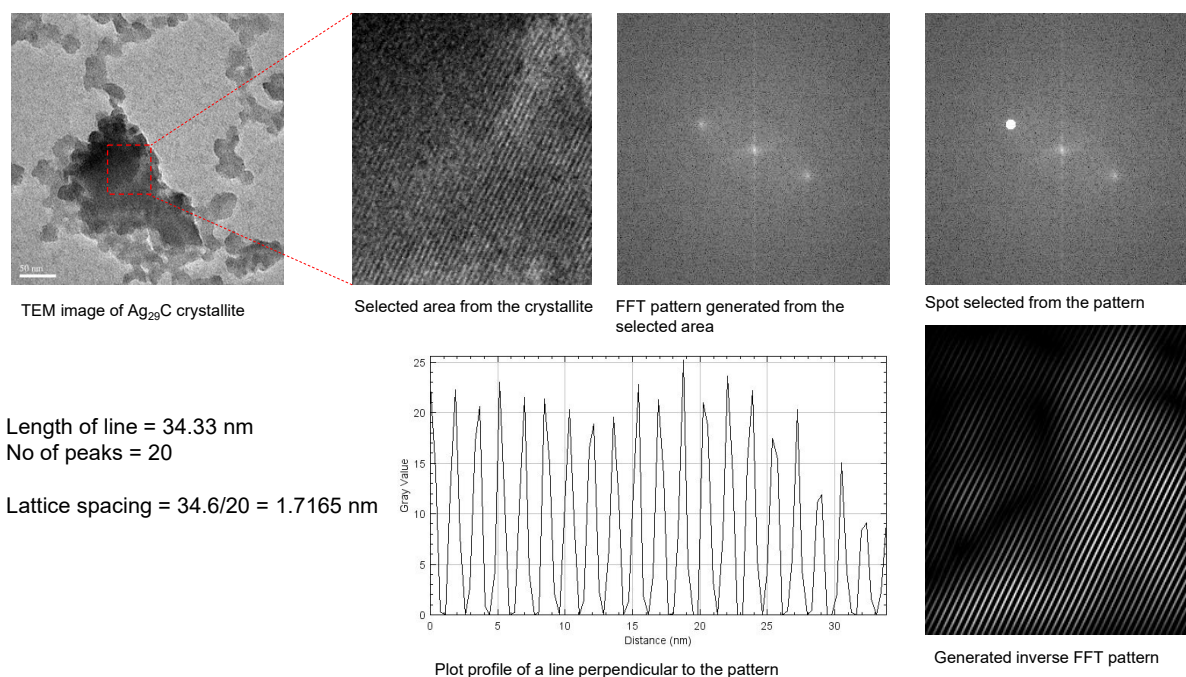


Fig. S15 Method used for calculating lattice distances from the experimental data.

References

- 1 L. G. AbdulHalim, M. S. Bootharaju, Q. Tang, S. Del Gobbo, R. G. AbdulHalim, M. Eddaoudi, D. Jiang and O. M. Bakr, *J. Am. Chem. Soc.*, 2015, **137**, 11970–11975.
- 2 C. P. Joshi, M. S. Bootharaju, M. J. Alhilaly and O. M. Bakr, *J. Am. Chem. Soc.*, 2015, **137**, 11578–11581.
- 3 A. Nag, P. Chakraborty, M. Bodiuzzaman, T. Ahuja, S. Antharjanam and T. Pradeep, *Nanoscale*, 2018, **10**, 9851–9855.